

Fig. 3. Power circuit diagram of the proposed super-high-speed PMSM drive.

and the operation of the current regulator was tested up to an excitation frequency of 1200 Hz. In addition, the vector control schemes with and without the discrete Hall sensors are proposed. In the case of a vector control with three discrete Hall sensors, the discrete Hall sensors provide rough position information with a resolution of $\pm 30^\circ$. Hence, the position estimator was proposed to derive the precise position.

In the proposed sensorless algorithm, the speed is estimated by processing the output voltage of the proportional and integral (PI) current regulator. The structure is simple and the estimated speed is robust to the measurement noise. The experimental system was built and the proposed controls were implemented and evaluated with and without the discrete Hall sensors. The test results, up to a speed of 65 000 r/min, are presented.

II. SYSTEM OVERVIEW

Fig. 1 shows the developed turbo-compressor system, and Fig. 2 shows the rotor assembly which is composed of a rotor, bearings, and two impellers. As shown in Fig. 2, two impellers are directly coupled to the left and right side of the rotor shaft. Air is compressed by the first impeller and it flows into the second impeller through the inter-cooler. Using two-stage impellers, the air pressure can be increased by up to 8 bar. In normal operation, the motor speed ranges from 60 000 to 70 000 r/min. The rotor diameter is less than 10 cm, but the rated power of motor is as high as 131 kW.

Fig. 3 shows the power circuit diagram of the developed super-high-speed PMSM drive. The parameters of the PMSM are described in Table I. In many conventional approaches, for the simplicity of current regulation, a buck or boost converter has been used to vary the dc-link voltage. However, in the proposed system, the constant dc link (600 V) through a simple diode rectifier is adopted for cost effectiveness and the reliability of the system. A dc-link inductor was used to improve the power factor of the utility source. In addition, three 1200-V 300-A insulated gate bipolar transistors (IGBTs) were connected in parallel to compose a switch for the inverter. The current rating of the power devices is much higher than that of the PMSM because the devices are derated in order to cope with the high switching frequency. A regenerative resistor was provided to prevent an overvoltage of the dc link, which can be caused by rapid motor deceleration. To achieve the sinusoidal current control up to the excitation frequency of 1200 Hz, the switching frequency of the inverter was set at 15 kHz. The high switching frequency increases the thermal dissipation of the

TABLE I
PARAMETERS OF PMSM

Number of Poles	2
Rated output [kW]	131
Rated speed [r/min]	70,000
Rated voltage [V_{rms}]	360
Rated torque [Nm]	17.9
Rated current [A_{rms}]	237
Stator resistor, R_s [Ω]	0.0055
Stator inductance, L_s [μ H]	28

devices and the thermal control is an important design issue. In the proposed system, watercooling was adopted for the thermal control of the stator of the PMSM and the inverter, and the rotor and bearings are cooled by the compressed air. By using watercooling, the physical size of the heat sink is remarkably smaller compared with that of an air-cooling system. The asymmetric Space-Vector pulsewidth modulation (SVPWM), which updates the PWM output twice per one PWM cycle, was applied and the control period was set to 33.33 μ s. Because the general-purpose microprocessors cannot meet the required calculation time, the TMS320VC33-150 digital-signal-processor (DSP)-based digital controller was developed for the implementation. The experimental data showed that it takes less than 20 μ s to perform the vector control scheme including the proposed sensorless algorithm. To measure the rotor angle, three discrete Hall-effect sensors with a sensing magnet were installed in the motor. These signals can provide the mechanical angle information with a resolution of 60° .

The PMSM was installed with special bearings for operations up to super-high speed. Because of the operational characteristics of the bearing, it is necessary to accelerate rapidly over the threshold speed range (about 6000–9000 r/min) in order to reduce mechanical wear.

III. DESIGN AND EVALUATION OF CURRENT REGULATOR

The synchronous reference frame current regulator has become the industry standard for regulating the current of polyphase ac machines due to its capability of regulating ac signals over a wide frequency range [5], [6]. In the proposed system, the design of a synchronous reference frame current regulator has been a challenging job due to the high dc-link

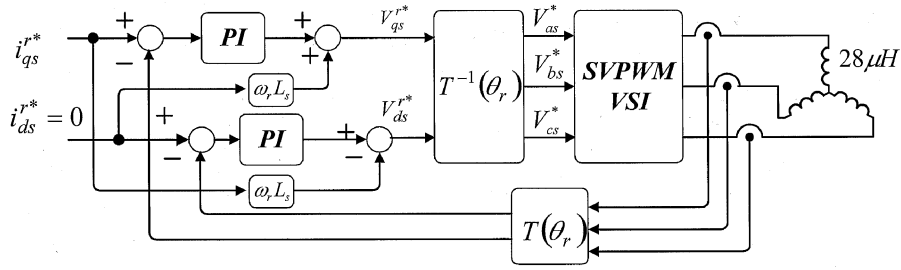


Fig. 4. Block diagram of the synchronous reference frame current regulator with the inductor.

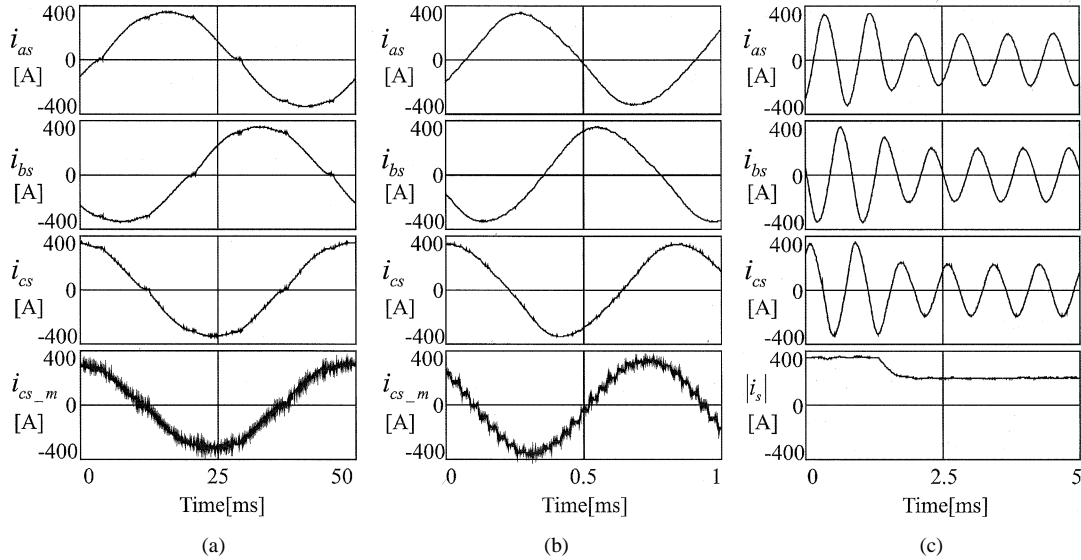


Fig. 5. Current waveform of synchronous reference frame current regulator with an inductor load. (a) Current waveforms with excitation frequency of 20 Hz. (b) Current waveforms with excitation frequency of 1200 Hz. (c) Current waveforms with excitation frequency of 1200 Hz. (Magnitude of current reference is changed from 350 to 200 A_{peak}).

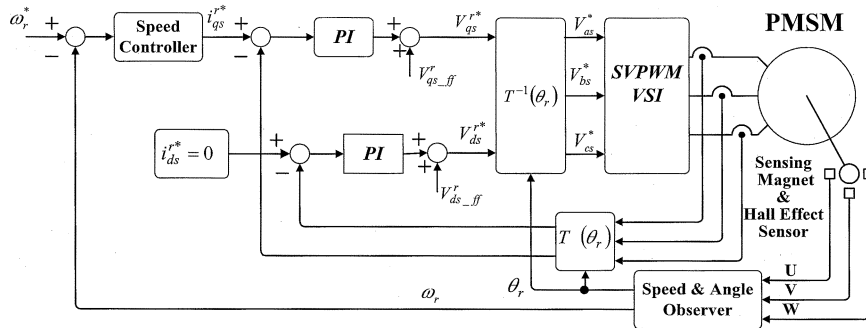


Fig. 6. Block diagram of the vector control scheme with the three discrete Hall-effect sensors.

voltage, the extremely small inductance, and the high power rating. In order to evaluate the feasibility of the synchronous reference frame current regulator, preliminary experiments were carried out with a three-phase inductor load, which has the same inductance value as the stator of a PMSM.

Because of the high power rating and high dc-link voltage, the dead time was set to 3 μs , which is relatively large considering the short PWM update period, 33.33 μs . Therefore, the precise compensation of the dead-time effect is a critical issue. For effective voltage synthesis with an SVPWM, the techniques reported in [7] and [8] were implemented. Because the ripple current is inevitably large, the precise current sampling is an

other important issue. The analog circuit was designed to avoid delay and noise.

Fig. 4 shows the block diagram of the synchronous reference frame current regulator with the inductor load. The transformation $T(\theta_r)$ is given by

$$\mathbf{T}(\theta_r) = \frac{2}{3} \begin{bmatrix} \cos \theta_r & \cos(\theta_r - \frac{2}{3}\pi) & \cos(\theta_r + \frac{2}{3}\pi) \\ -\sin \theta_r & -\sin(\theta_r - \frac{2}{3}\pi) & -\sin(\theta_r + \frac{2}{3}\pi) \\ \frac{1}{\sqrt{2}} & \frac{1}{\sqrt{2}} & \frac{1}{\sqrt{2}} \end{bmatrix} \quad (1)$$

where the angle θ_r is the angle between the synchronous reference frame and the stationary frame.

Fig. 5 shows the experimental results with the proposed current regulator. A three-phase air-core reactor is used for the test, and the inductance is set to the same value of the stator inductance of the PMSM, $28 \mu\text{H}$.

From the top to bottom, the traces show the three phase currents sampled by the controllers, i_{as}^r , i_{bs}^r , i_{cs}^r , and the c -phase current measured by the current probe set (Tektronix CT-4, A6302 and AM503), i_{cs-m} . The traces shown in Fig. 5(a) present the experimental results using an excitation frequency of 20 Hz. From the results shown in Fig. 5(a), it can be seen that the performance of the current regulator was degraded at the zero crossings of the phase currents because of the effect of the dead time and the zero-current clamping even after careful compensation [7], [8], [10]. The traces in Fig. 5(b) show the experimental results with an excitation frequency of 1200 Hz. Because the dead-time effect and the zero-current clamping effect are reduced at high frequency, the currents are well controlled sinusoidally without degradation. However, the measured currents i_{cs-m} in Fig. 5(a) and (b) show large ripples due to the very small load inductance. The delay in the sampled current i_{cs} to the measured current i_{cs-m} is caused by a delay in the serial D/A converter and the low-pass filter circuit. The traces in Fig. 5(c) show the dynamic characteristic of the current regulator at a frequency of 1200 Hz. The magnitude of the current reference was changed from $350 A_{\text{peak}}$ to $200 A_{\text{peak}}$. The bottom trace in Fig. 5(c) shows the magnitude of the current vector, $|i_s|$. The three phase currents are well regulated sinusoidally over a wide frequency range by the synchronous current regulator, and the response is sufficiently fast for the application.

IV. VECTOR CONTROL SCHEME WITH THREE DISCRETE HALL-EFFECT SENSORS

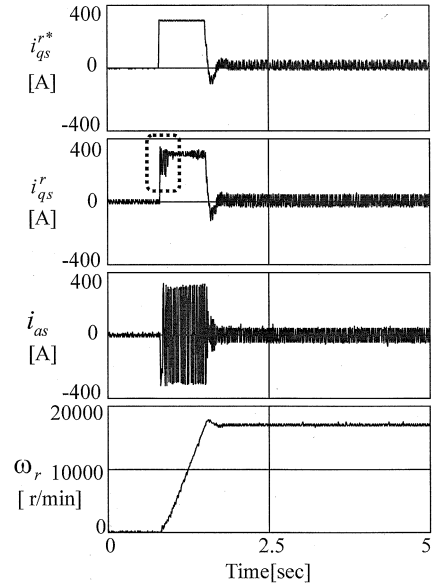
Fig. 6 shows a block diagram of the vector control scheme with three Hall sensors. In the block diagram, the feedforward terms $V_{ds\text{-ff}}^r$, $V_{qs\text{-ff}}^r$ for the decoupling control are given by

$$V_{ds\text{-ff}}^r = -L_s \omega_r i_{qs}^{r*} \quad (2)$$

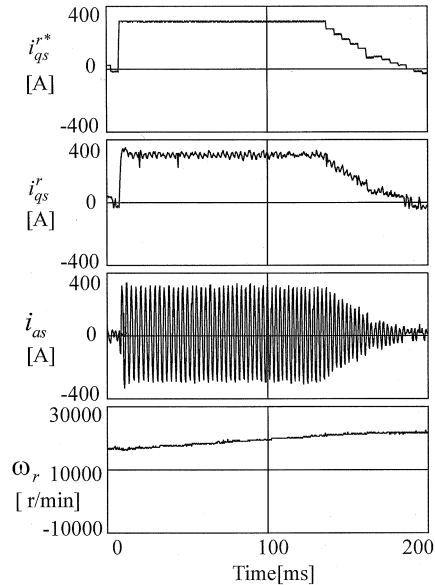
$$V_{qs\text{-ff}}^r = L_s \omega_r i_{ds}^{r*} + \omega_r \lambda_f \quad (3)$$

where λ_f is the back electromotive force (EMF) constant of the PMSM.

In the proposed system, the information on the rotor angle is provided by three discrete Hall-effect sensors with a sensing magnet. The Hall-effect sensors provide the absolute angle information with a resolution of $\pm 30^\circ$. Because the resolution is not sufficiently accurate for the vector control, the resolution of the angle information was enhanced by extrapolating the angle using the time and speed information. Fig. 8 shows the relationship between the angle pulse and the sampling point for the current control. The duration time T from the input of the latest angle pulse to the sampling point was measured by the programmable logic device. The speed of the motor, ω_r , can be calculated using the conventional method from the count and period of the pulses provided by the Hall-effect sensors [11].



(a)



(b)

Fig. 7. Acceleration characteristics of the PMSM with the vector control scheme using the three discrete Hall sensors. (a) Acceleration from zero speed to 17 000 r/min. (b) Acceleration from 17 000 to 20 000 r/min.

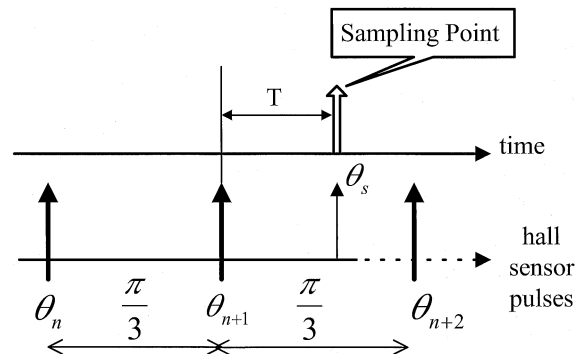


Fig. 8. Extrapolation of the angle using time and speed information.

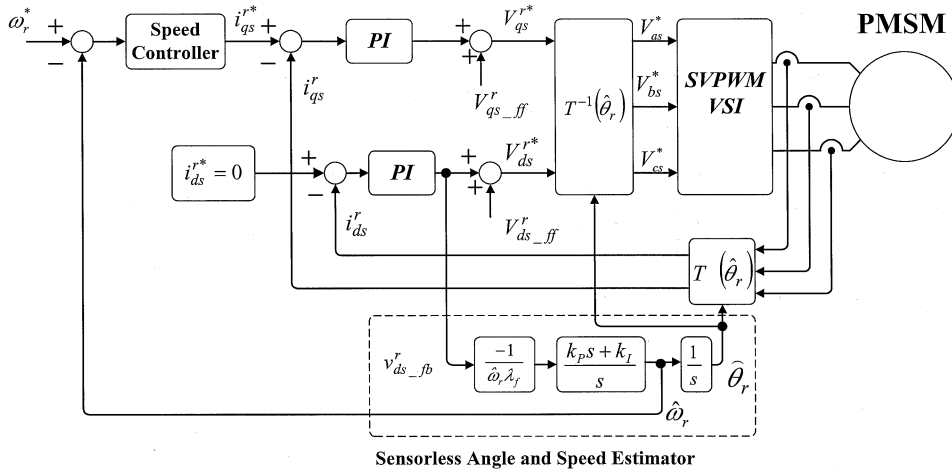


Fig. 9. Block diagram of sensorless vector control scheme without position sensor.

Based on the assumption that the rotor speed does not change between the pulses, the rotor angle at the sampling point θ_s can be derived as follows:

$$\theta_s = \theta_n + T \cdot \omega_r \quad (4)$$

where θ_n is the rotor angle at the latest pulse.

Because the period of the pulse is less than 200 μ s at the normal speed and the speed does not change rapidly, reasonably accurate speed information can be calculated by the algorithm.

The test results with the proposed vector control scheme using the angle information of the Hall-effect sensors are shown in Fig. 7. For the experiment, three discrete Hall-effect sensors with a sensing magnet were installed in the PMSM and a special digital logic circuit was implemented to measure the angle θ_n and the time T of Fig. 8 using the programmable logic device.

From top to bottom, the traces show the q -axis current reference i_{qs}^{r*} , the q -axis current i_{qs}^r , the motor phase current i_{as} , and the rotor speed ω_r . Fig. 7(a) shows the acceleration from zero to 17000 r/min. The results indicate that the current is well regulated and the rotor accelerates rapidly up to the threshold speed of the bearing. However, in the dotted-line square, large current ripples of the q -axis current are shown. For the test, the extrapolation of the rotor angle has not been carried out at low speed, where the speed information is not reliable. Therefore, the discontinuous angle information deteriorated the performance of the current regulator. Fig. 7(b) shows the acceleration from 17000 to 20000 r/min. Because precise angle information is available using the extrapolation, the vector control scheme provides the effective current and speed regulation.

Compared to the conventional position sensors, the discrete Hall sensors were much more reliable in a super-high-speed operation. However, the installation of the Hall sensors and the sensing magnet limits the mechanical design, and the sensorless control is a better solution for super-high-speed applications. In the case of the turbo-compressor application, the installation of a sensing magnet even causes difficulties in the aerodynamic design.

V. SENSORLESS VECTOR CONTROL SCHEME WITHOUT ANY POSITION SENSOR

Fig. 9 shows a block diagram of the sensorless vector control scheme without the position sensor. In the diagram, the feedforward terms $V_{ds_ff}^r$, $V_{qs_ff}^r$ for the decoupling control are given by

$$V_{ds_ff}^r = R_s i_{ds}^{r*} - L_s \hat{\omega}_r i_{qs}^{r*} \quad (5)$$

$$V_{qs_ff}^r = R_s i_{qs}^{r*} + L_s \hat{\omega}_r i_{ds}^{r*} + \hat{\omega}_r \lambda_f \quad (6)$$

where $\hat{\omega}_r$ is the estimated rotor speed.

Neglecting the electrical transient, the voltage equations of the PMSM in the estimated reference frame can be presented by

$$v_{ds}^r = R_s i_{ds}^r - \omega_r L_s i_{qs}^r + \omega_r \lambda_f \sin \theta_{err} \quad (7)$$

$$v_{qs}^r = R_s i_{qs}^r + \omega_r L_s i_{ds}^r + \omega_r \lambda_f \cos \theta_{err} \quad (8)$$

where the angle error θ_{err} is the error between the real rotor angle θ_r and the estimated angle $\hat{\theta}_r$

$$\theta_{err} = \hat{\theta}_r - \theta_r. \quad (9)$$

From the relationship between (5) and (7), the d -axis voltage error, which has to be compensated for by the d -axis PI regulator, can be derived as follows:

$$v_{ds_error}^r = R_s (i_{ds}^r - i_{ds}^{r*}) - \omega_r L_s (i_{qs}^r - i_{qs}^{r*}) + \omega_r \lambda_f \sin \theta_{err}. \quad (10)$$

Considering that the currents are regulated by the current regulator without significant errors and the angle error θ_{err} is small, the output voltage of the d -axis PI compensator can be expressed as follows:

$$\begin{aligned} V_{ds_fb}^r &\approx v_{ds_error}^r \\ &\approx \omega_r \lambda_f \sin \theta_{err} \\ &\approx \omega_r \lambda_f \theta_{err}. \end{aligned} \quad (11)$$

In the proposed estimator in Fig. 9, the error signal of (11) is processed by the PI compensator to derive the rotor speed and the rotor angle is calculated by integrating the estimated speed. In the conventional method [3], a differentiation process

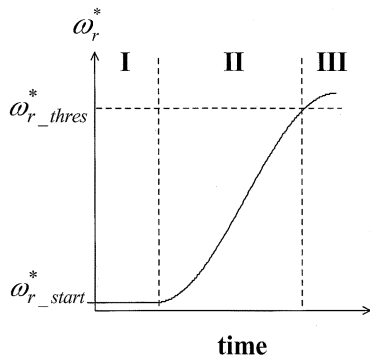


Fig. 10. Frequency pattern for constant current control with pre-patterned frequency.

is used to calculate the speed but this makes the system vulnerable to measurement noise. The experimental study reveals that the proposed estimator provides a very accurate and robust speed information for the application. However, at the zero and low speed, the back-EMF voltage is not high enough for the proposed vector control. Hence, for the initial alignment and starting from zero speed, the current was controlled with a constant magnitude using a pre-patterned angular frequency. In addition, the angle for the synchronous reference frame was calculated by integrating the frequency. Fig. 10 shows the frequency pattern for the initial alignment and starting. As shown in step I of Fig. 10, the initial value of the frequency pattern is set to a small but constant speed $\omega_{r_start}^*$ for the initial rotor alignment. After the alignment, according to the speed pattern in step II, the motor is accelerated up to the threshold speed $\omega_{r_thres}^*$. Over the threshold speed, the motor is then controlled by the proposed sensorless control and the speed is estimated by the proposed estimator shown in Fig. 9.

VI. EXPERIMENTAL RESULTS WITH SENSORLESS CONTROL

The experimental results with the proposed sensorless control are shown in Figs. 11–14. Fig. 11 shows the starting characteristics from zero speed to 20 000 r/min. The PMSM was accelerated by the rotating current vector with the precalculated frequency pattern shown in Fig. 10. In order to align the rotor, the current vector was rotated with the starting frequency $\omega_{r_start}^* = 2\pi$ rad/s, as shown in step I. The proposed sensorless control of step III was activated from 12 000 r/min and the speed was estimated. The bottom trace of Fig. 11 shows the measured speed using the Hall-effect sensors. The test results in Fig. 11 reveal that the PMSM is effectively accelerated up to a threshold speed according to the proposed starting sequence and that the speed is well estimated by the proposed sensorless algorithm.

Fig. 12 shows the acceleration characteristics from 58 000 to 60 000 r/min. The torque component current was well controlled and the phase current was harnessed without overshoot using the synchronous current regulator. In addition, the results show that the proposed control has sufficient speed control dynamics for the turbo-compressor.

Fig. 13 shows the performance of the current regulator using the proposed sensorless control. For the experiments, the bandwidth of the current regulator was set to 3,000 rad/s. The current

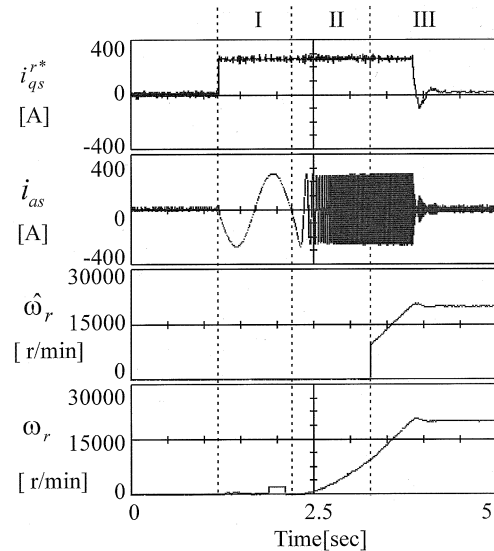


Fig. 11. Starting characteristics of the PMSM with sensorless vector control scheme.

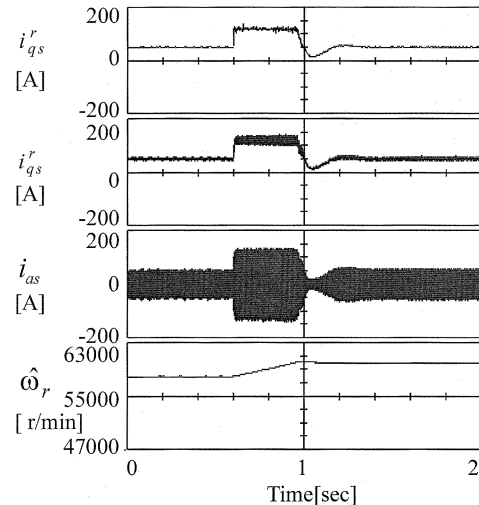
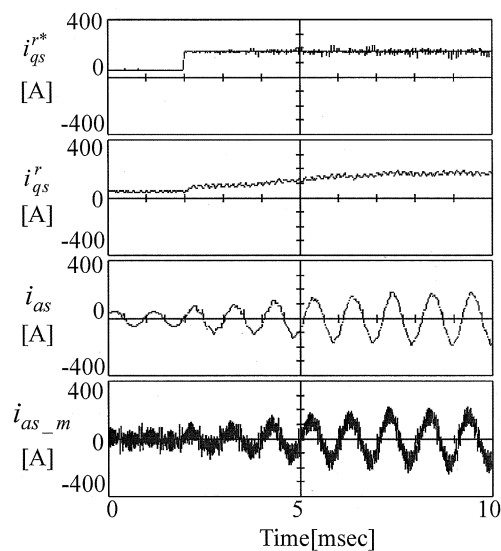


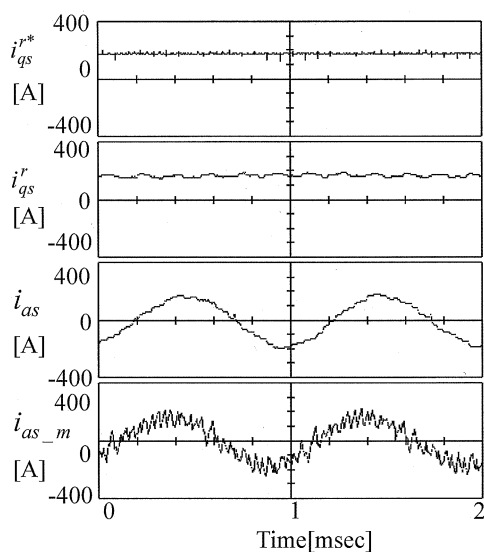
Fig. 12. Acceleration characteristics of the PMSM with the sensorless vector control scheme. (From 58 000 to 60 000 r/min).

was measured at the acceleration from 58 000 to 60 000 r/min. As shown in Fig. 13(a), despite the high excitation frequency of 1 kHz, the q -axis current i_{qs}^r tracks the command with a small ripple current, which is caused by the dead time and zero-current clamping effects. Because the current control bandwidth was set low for the sensorless algorithm, the actual current tracks the command with a delay. The bottom trace shows the measured phase current, i_{as-m} , which was measured by a current probe set (Tektronix AP504CX and AM503B). Due to the extremely small stator inductance, the fundamental current was accompanied by a significant ripple current, which was caused by the 15-kHz PWM switching. Fig. 13(b) shows the magnified waveforms of the last two periods in Fig. 13(a). The traces show that the phase current is controlled sinusoidally by the precise sampling of the fluctuating current.

In Fig. 13, the measured phase current i_{as-m} shows a relatively large current ripple, which can increase the temperature of the rotor. Because a high temperature can degrade the



(a)



(b)

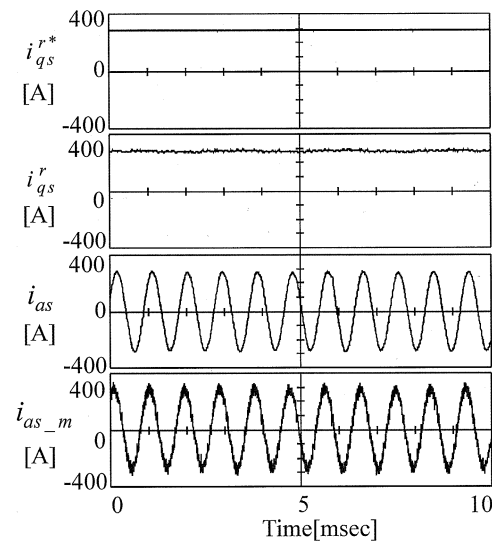
Fig. 13. Current waveforms with the proposed sensorless control (acceleration from 58 000 to 60 000 r/min). (a) Current waveforms. (b) Magnified figures of the last two periods of current waveforms in (a).

mechanical stability of the rotor, it is desirable to reduce the current ripple. Fig. 14 shows the current waveforms with a $28\text{-}\mu\text{H}$ external inductor to reduce the current ripple. The waveforms show that the current is well regulated sinusoidally at a speed of 65 000 r/min with an output power of 120 kW. The measured phase current, i_{as-m} , shows that the current ripple is reduced remarkably by the external inductor.

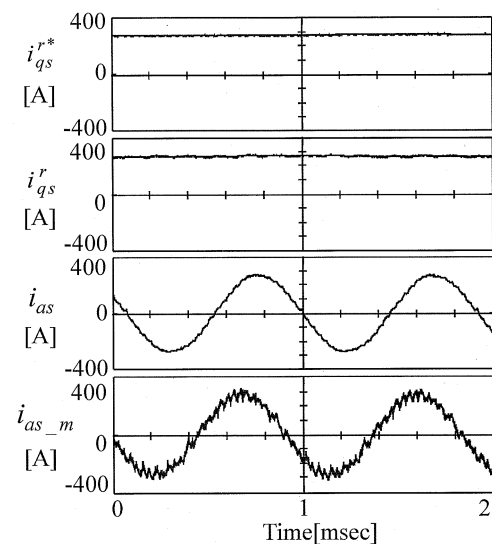
As shown in Fig. 14, the current ripple can be easily reduced by the external inductor. However, because the adoption of an external inductor requires a higher inverter output voltage, the value of the inductor can be determined by a tradeoff between the current waveform and the inverter output voltage capability.

VII. CONCLUSION

The development of a super-high-speed drive for a 131-kW 70 000-r/min PMSM for use in a turbo-compressor was dis-



(a)



(b)

Fig. 14. Current waveforms with an external inductor of $28\text{ }\mu\text{H}$ (at speed of 65 000 r/min). (a) Current waveforms. (b) Magnified waveforms.

cussed. The synchronous reference frame current regulator was implemented with challenging requirements such as a low stator inductance ($28\text{ }\mu\text{H}$) and a high dc-link voltage (600 V). The experimental results of the current regulator operating up to 1200 Hz were presented. To overcome the problem of the position sensor for the super-high-speed operation, a new vector control scheme without a position sensor was proposed. In this scheme, a new position and speed estimator was derived. The proposed estimator can provide reliable angle and speed information, which is robust to the measurement noise. The experimental results of the sensorless vector control scheme operating up to 65 000 r/min illustrated the validity of the proposed control scheme.

REFERENCES

- [1] S. L. Hamilton, "Micro turbine generator program," in *Proc. 33rd Annu. Hawaii Int. Conf. System Sciences*, 2000, p. 103.

